Combustion and Flame 201 (2019) 160–169

Contents lists available at ScienceDirect

Combustion and Flame

journal homepage: www.elsevier.com/locate/combustflame

Flame propagation in nano-aluminum–water (nAl–H_2O) mixtures: The role of thermal interface resistance

Murali Gopal Muraleedharan[a], Umesh Unnikrishnan[a], Asegun Henry[b], Vigor Yang[a,*]

[a] School of Aerospace Engineering, Georgia Institute of Technology, Atlanta, GA 30332, USA
[b] Department of Mechanical Engineering, Massachusetts Institute of Technology, Cambridge, MA 02139, USA

ARTICLE INFO

Article history:
Received 29 September 2018
Revised 4 November 2018
Accepted 18 December 2018
Available online 31 December 2018

Keywords:
Heat transfer
Conduction
Aluminum
Thermal interface resistance
Modeling
Flame

ABSTRACT

A detailed numerical analysis of flame propagation in nano-aluminum–water (nAl–H_2O) mixture is performed. Emphasis is placed on investigating the role of particle thermal conductivity in the prediction of the burning properties of the mixture. Flame structure and burning characteristics are obtained by solving the energy equation using finite difference discretization and the Gauss–Seidel iteration method. Particle thermal conductivity is modeled using the temperature-dependent thermal conductivities of the aluminum core and oxide layer, as well as their interface resistance. The effective thermal conductivity of the mixture is modeled as a function of temperature, spatial coordinate, and local mixture composition, by means of the unified Maxwell–Eucken–Bruggeman model, accounting for random particle distribution and inter-particle interaction. Results indicate that the combined thermal resistance offered by the oxide layer and the interface constitute 95% of the total resistance of the particle. The calculated particle-size dependent linear burning rates show good agreement with experimental data, with only 5% error. Error in burning rate prediction increases, however, to 20% when interface resistance is excluded from the particle thermal conductivity model. It was also observed that burning rate varies as the inverse of particle size. Finally, an analysis of the sensitivity of burning rate to the individual components of the particle thermal conductivity model is also performed. Results suggest a 30% decrease in burning rate for two orders of magnitude reduction in both interface conductance and oxide thermal conductivity. The burning rate drops by only 15%, however, for a similar reduction in aluminum thermal conductivity. A heat conduction perspective on flame propagation in nanocomposites is presented, identifying the highest and the lowest conductive pathways for energy transport.

1. Introduction

Metal-based energetic materials have received considerable attention in space and underwater propulsion [1,2], explosives [3], and hydrogen generation [4]. Among the metals, aluminum (Al) is particularly attractive, due to its abundance, low cost of extraction, high volumetric energy density, and environmentally safe combustion products [5,6]. Composites containing meso- and micron-sized Al particles have offered excellent performance in space propulsion applications since the 1950′s [1,7]. In the last two decades, however, nanosized aluminum (nAl) particles (< 100 nm in size) have been preferred over larger Al particles, owing to their superior burning characteristics [8–10]. As compared with bulk Al, nAl offers enhanced combustion efficiency due to their higher specific surface area (SSA) [11], lower melting and boiling temperatures [12], reduced ignition time and temperature [10], and higher reaction rates [10,13].

Despite distinct advantages, however, the low thermal conductivity of nanoparticles [14–16] impedes the extensive use and commercialization of nano-energetic mixtures. Reduced energy transport rates have adverse effects on their combustion and ignition properties. For instance, the linear burning rate, r_b of such mixtures varies roughly as the square root of mixture thermal conductivity, k_m [5,6,8]. A 10% reduction in k_m, therefore, reduces r_b by 5%, resulting in reduced specific impulse and thrust. Combustion of Al particles smaller than 10 μm in size has shown significant deviation from the classical D^2 law and the burning time was linearly dependent of the particle size [5,8]. This is in contradiction with the continuum models which suggest that the combustion of nAl particles is dictated by mass-diffusion, and the burning time should be quadratically proportional to the particle diameter. Moreover, the burning time tends to decrease with increasing pressure, suggesting a kinetically-controlled combustion. These experimental observations suggest that nAl

* Corresponding author.
E-mail address: vigor.yang@aerospace.gatech.edu (V. Yang).

https://doi.org/10.1016/j.combustflame.2018.12.022
0010-2180/

particles undergo an ignition mechanism wherein the reactions leading to ignition follow melting of aluminum core [8,10,17,18]. Melting of core escalates internal pressure, subsequently cracking the oxide shell. Ignition reactions occur in these cracks following inter-diffusion of reactant species. Therefore, heat conduction from the reaction zone upstream is essential in raising the temperature of particles to the melting point of aluminum.

Understanding the nanoscale thermal transport behavior is, therefore, crucial in elucidating the burning behavior of nano-energetic mixtures. Note that, owing to the high reactivity with atmospheric oxygen, the Al surface is usually covered with a 2-3 nm thick coating of aluminum oxide (Al_2O_3). While Al is a good heat conductor, Al_2O_3 is an insulator. Thus, the thermal conductivity of Al_2O_3 at room temperature is ~30 W/m K, which is nearly one-eighth that of Al (~230 W/m K). Since both the Al core and Al_2O_3 layer are of nanoscale dimensions, thermal conductivity could be affected by their size. Thermal conductivity of nanostructure could be several orders of magnitude lower than its bulk counterpart due to the effect of excessive boundary scattering on heat carriers (electrons and phonons) [16,19,20].

In addition, the Al/Al_2O_3 interface also poses resistance to heat conduction. To characterize the heat lost at the interface, thermal interface resistance (TIR) (denoted by R) may be used. TIR is the inverse of thermal interface conductance (TIC) (denoted by G), which is the constant of proportionality in the equation that relates heat flux (Q) across the interface of two materials to the temperature drop (ΔT) at the interface ($Q = G\Delta T = \Delta T/R$). Although TIR is present at all material interfaces, its effects are stronger as the particle size decreases, that is, as the percentage of surface atoms increases [16]. Prior work has shown that for nanoparticles of sizes < 100 nm, more than 90% of the total thermal resistance of the particle originates from the interface [21,22]. TIR of Al/Al_2O_3, however, has not been widely studied. To our knowledge, there are only three experimental measurements on the temperature dependence of TIR reported in the literature [23–25], and these measurements were in the temperature range of 50–480 K. High temperature measurement of TIR is intrinsically challenging, even under near-vacuum conditions, because of the high reactivity and vaporability of Al atoms.

Due to the limited understanding of interfacial heat transport, prior studies on the combustion characteristics of nAl suspensions have not accounted for the effect of TIR on burning properties. Tyagi et al. [26] measured the ignition probability of diesel droplets laden with nAl particles of 50 nm diameter. The measured ignition probability suggested a 100% enhancement with addition of nanoparticles, and this was ascribed partly to the enhanced radiative and heat transfer properties of nAl-laden fluids. Nonetheless, a systematic analysis of the effect of TIR was not performed. Risha et al. [27,28] considered a suspension of nAl particles dispersed in water and studied the effects of pressure and particle size on the burning characteristics. Measurements spanned a pressure range of 0.1–10 MPa. Particles of sizes 38–130 nm were considered. The measured burning rate was inversely proportional to the particle diameter, and the pressure exponent was in the range of 0.27–0.47, depending on the particle size. Complementing the experiments of Risha et al. [27,28], a theoretical study was also performed by Sundaram et al. [10] to model flame propagation in these mixtures. They adopted a modeling approach followed for micron-sized particle mixtures, using approximate thermal transport property models that do not take TIR into consideration. As a result, they severely overpredicted linear burning rate, r_b in these systems. For instance, mean error in r_b for 130 nm particle is ~25%, whereas for the 80 nm particle, this increases to 31%. For 38 nm particle suspensions, the predicted quantitative and qualitative trends were much different from experimental results. Furthermore, the mean error was more than 50%, with a peak error in r_b being

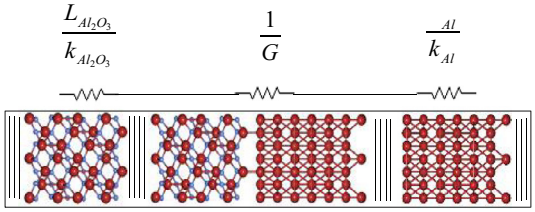

Fig. 1. Series circuit framework for evaluating thermal conductivity of nanoparticle.

104% at 3.5 MPa. They attributed this to the adsorption of water molecules to the nanoparticle surface, and argued that it prevents the diffusion of oxidizer molecules toward the core Al atoms. While this is a plausible claim, recent studies [8] indicate that mass diffusion is not a rate-limiting process in the combustion of nAl suspensions. Hence, we hypothesize that this disparity was due to oversimplification of nanoscale heat conduction physics and inadequate modeling of the thermal conductivity of the system.

The primary objective of the present work is, therefore, to systematically investigate the role of thermal resistance offered by Al, Al_2O_3, and the interface in modeling effective thermal conductivity, and subsequently, flame propagation in a nAl–H_2O mixture. Here, we quantitatively evaluate the TIR of Al/Al_2O_3 using the recently reported interfacial conductance modal analysis (ICMA) technique, [29] within a framework of equilibrium molecular dynamics simulations for temperatures ranging from 300 to 1800 K. The size effects of thermal conductivities of Al and Al_2O_3 are also quantified using the thermal conductivity accumulation functions evaluated from first-principle lattice dynamics calculations, along with the solution of Boltzmann transport equations (BTE) [30,31]. Following the TIR calculations, effective thermal conductivity of the suspension is modeled by taking into account the effect of particle size, temperature, and random dispersion in the mixture. Finally, the effective thermal conductivity model is applied in combination with the particle burning time scales to simulate a vertically propagating one-dimensional flame in a stoichiometric mixture under isobaric conditions. Thermal properties are assumed to be spatially varying, and the nonlinear energy equation is solved iteratively to obtain steady state solutions. Linear burning rate, r_b is computed, and the effect of particle size is also assessed. Finally, the sensitivity of r_b to variations in transport properties is also analyzed to provide a heat conduction perspective on combustion of metal-based nano-energetic materials.

2. Effective thermal conductivity model

The inputs of an effective thermal conductivity model are the particle thermal conductivity (k_p), fluid thermal conductivity (k_f), and the particle volume fraction, ϕ. In order to evaluate k_p, consider a series circuit model representing the interface of Al and Al_2O_3, as shown in Fig. 1.

This circuit is a partial representation of the nano-aluminum particle with oxide coating. It consists of three main components: bulk Al, whose thermal conductivity is denoted by k_{Al}, bulk Al_2O_3, whose thermal conductivity is denoted by $k_{Al_2O_3}$, and the interfacial device, whose conductance is denoted by G. As shown in Fig. 1, the thermal resistance from Al_2O_3, Al, and the interface are given as: $\frac{L_{Al_2O_3}}{k_{Al_2O_3}}$, $\frac{L_{Al}}{k_{Al}}$, and $\frac{1}{G}$, respectively. L denotes the length of each device. The net thermal conductivity of the interfacial system, k_{int}, shown in Fig. 1, can be obtained as:

$$k_{int} = \frac{L}{\left(\frac{L_{Al_2O_3}}{k_{Al_2O_3}} + \frac{L_{Al}}{k_{Al}} + \frac{1}{G}\right)} \quad (1)$$

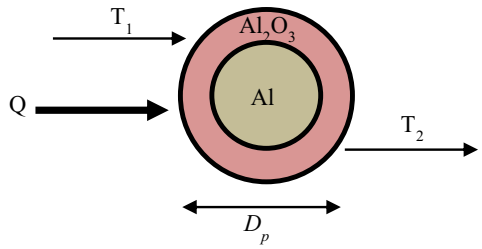

Fig. 2. Schematic diagram of the core-shell particle model for evaluating the effective thermal conductivity of a nanoparticle.

With the core-shell particle model shown in Fig. 2, this concept can be extended to estimate the thermal conductivity, k_p of a passivated nAl particle with a total diameter D_p as:

$$k_p = \frac{D_p}{\left(2.\frac{L_{Al_2O_3}}{k_{Al_2O_3}} + \frac{L_{Al}}{k_{Al}} + \frac{2}{G}\right)}. \tag{2}$$

The temperature dependent bulk thermal conductivities of Al and Al_2O_3 are experimentally evaluated and documented [32,33]. Note, however, that both the Al core and the Al_2O_3 layer could be affected by their sizes. In our prior work, we have introduced a method based on first-principle lattice dynamics calculations, along with the solution of the phonon Boltzmann transport equation, to gauge the effect of particle size on phonon thermal conductivity by obtaining the thermal conductivity accumulation function [30]. This method can be used to quantify the size effect on the phonon thermal conductivities of Al and Al_2O_3. Our analysis indicates that Al particles of dimension less than 34 nm and Al_2O_3 particles less than 47 nm are affected by size, as shown in Fig. 3.

Likewise, Jain and McGaughey [31] have obtained the electron thermal conductivity accumulation function on Al to identify that particles with dimensions less than 23 nm are affected by size. By combining these two results, we have developed a size-affected thermal conductivity model for Al and Al_2O_3 as given by the following equations:

$$\begin{aligned} k &= k_{bulk}, D \geq L_{\max} \\ k &= \left(\frac{D}{L_{\max}}\right) k_{bulk}, D < L_{\max} \end{aligned} \tag{3}$$

where D is the particle size (diameter for Al or thickness for Al_2O_3), $L_{\max} = 34$ nm (phonon) and 23 nm (electron) for Al, and 47 nm (phonon) for Al_2O_3. Electron thermal conductivity in Al_2O_3 is negligible because of the large bandgap between valence and conduction bands.

Following this, the TIC at the Al/Al_2O_3 interface was evaluated using the ICMA technique. With the use of the approach of Barrat et al. [34] and Domingues et al. [35], the instantaneous heat flow across the interface can be obtained as follows. In a microcanonical ensemble, the rate at which energy transmitted across the boundary of material A is equal to the rate of change of energy in material B (where A and B form the interface), at any instant. From statistical mechanics, the Hamiltonian, H, of such a system is:

$$H = \sum_{i}^{N} \frac{\mathbf{p}_i^2}{2m_i} + \Phi(\mathbf{r}_1, \mathbf{r}_2, \ldots, \mathbf{r}_n) \tag{4}$$

where $\boldsymbol{p}$ is the momentum and m the mass of atom i, and Φ the potential energy of the n-particle system. The Hamiltonian of an individual atom thus becomes

$$H_i = \frac{\mathbf{p}_i^2}{2m_i} + \Phi_i(\mathbf{r}_1, \mathbf{r}_2, \ldots, \mathbf{r}_n) \tag{5}$$

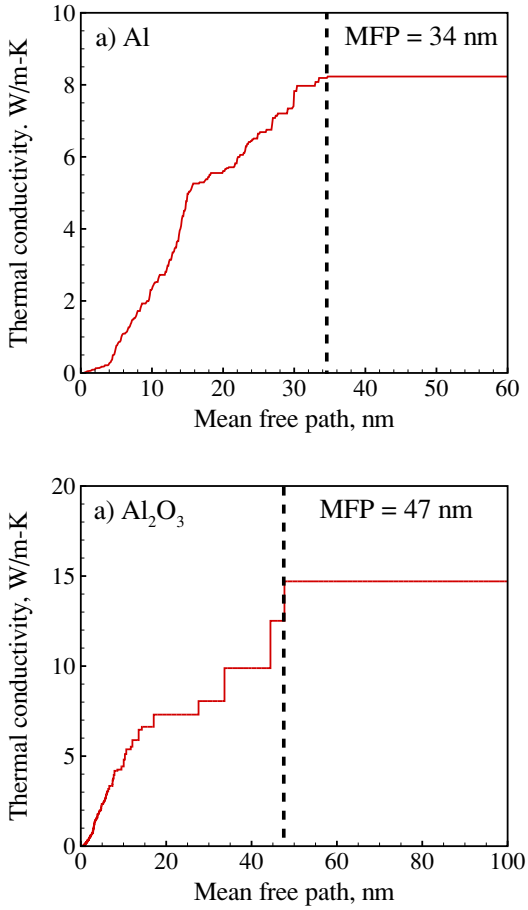

Fig. 3. Phonon thermal conductivity accumulation functions of (a) Al and (b) Al_2O_3.

The instantaneous energy transfer across the interface of A and B, $Q_{A\to B}$ can be expressed as:

$$Q_{A\to B} = -\sum_{i\in A}\sum_{j\in B}\left\{\frac{p_{i,\alpha}}{m_i}\left(\frac{-\partial H_j}{\partial \mathrm{r}_i}\right) + \frac{p_{j,\alpha}}{m_j}\left(\frac{\partial H_i}{\partial \mathrm{r}_j}\right)\right\} \tag{6}$$

where r is the position vector of atom represented by i and j. From this relation, using the fluctuation-dissipation theorem, [36] the total conductance of the interface can be calculated via correlation in the equilibrium fluctuations of the heat flow as:

$$G = \frac{1}{Ak_BT^2}\int \langle Q(t)\cdot Q(0)\rangle dt \tag{7}$$

Thermal interface resistance, R is evaluated as $R = 1/G$

Now that we have obtained all the necessary ingredients in Eq. (2) to evaluate k_p, the next step is to model the effective thermal conductivity of the mixture, k_m. There are several effective thermal conductivity models for nanoparticle suspensions [37–39]. Some of them are based on *dynamic* heat conduction mechanisms [40] in nanofluids, namely base-fluid nanolayering and Brownian motion. In a recent study on thermal conductivity of nano-suspensions, Muraleedharan et al. [41] conducted molecular dynamics simulations in combination with fluctuation-dissipation theorem to rigorously show that nanolayering and Brownian motion make negligible contributions to the effective thermal conductivity of the mixture. Therefore, in this work, we have neglected these effects. Two other important factors to be considered in modeling k_m of a dense suspension are the random particle distribution and the viscous interaction between nanoparticles. The Maxwell–Eucken [42–44] effective medium theory properly accounts for the random distribution of particles, and can be given

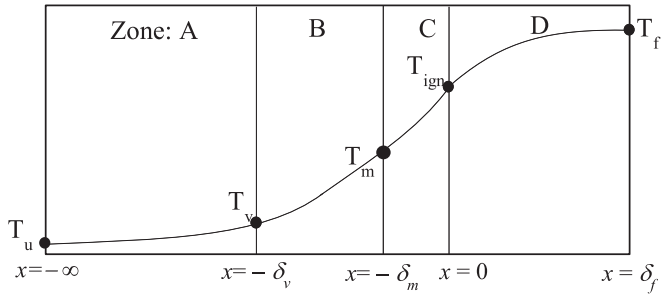

Fig. 4. Theoretical multizone framework used to represent reaction and preheat zones. Zones A–C represent preheat zones and Zone D represents the reaction zone.

as:

$$k_m = \frac{\phi_f k_f + \phi_p k_p \left(\frac{3k_f}{2k_f + k_p}\right)}{\phi_f + \phi_p \left(\frac{3k_f}{2k_f + k_p}\right)}, \tag{8}$$

where k_f is the fluid thermal conductivity, and ϕ_f and ϕ_p the volume fractions of fluid and particle, respectively. Interaction between particles is also important in capturing the viscous effects in the system, and can be accommodated by using the Bruggeman effective medium theory [45], as given by:

$$\phi_p \left(\frac{k_p - k_m}{k_p + 2k_m}\right) + \phi_f \left(\frac{k_f - k_m}{k_f + 2k_m}\right) = 0 \tag{9}$$

Therefore, in order to include both these effects, it is desirable to unify the Maxwell–Eucken and Bruggeman theories into a Maxwell–Eucken–Bruggeman (MEB) model, yielding effective thermal conductivity of the mixture, k_m, as:

$$k_m = \frac{D + \sqrt{D^2 + 2k_p k_f}}{2}, \tag{10}$$

where

$$D = (2k_p - k_f)\phi_p(1 - \alpha_p) + (2k_f - k_p)\phi_f \left(\frac{2\phi_f + 2\phi_p \alpha_p - 1}{2\phi_f}\right). \tag{11}$$

Here α_p is the volume fraction of particles in a mixture with a Maxwell–Eucken structure. The value of α_p is chosen to be 0.5 so as to conform to the condition that for $\phi_p \to 1$, $k_m \to k_p$.

3. One-dimensional flame model and numerical framework

A one-dimensional, isobaric flame propagating vertically downward through a stoichiometric mixture of nano-aluminum particles and liquid water is considered. This represents the real physical system on which combustion experiments were performed, and results are available for validation [28]. The particles are assumed to be fully dispersed (or non-agglomerated) and spherical with a monomodal distribution. A multi-zone framework representing the flame and preheat zones is shown in Fig. 4.

As can be seen from Fig. 4, several distinct zones can be identified within the framework. Zone A represents the nAl–H_2O (l) reactant mixture, which constitutes the propellant pellet originally synthesized for experimental study. The initial temperature of the unburnt propellant, T_u, may be conveniently assumed to be ambient temperature, $T_u = 298$ K. In Zone A, the major physical process is the heating of the system from T_u to the vaporization temperature of water, T_v, and there are no notable chemical reactions in this zone, due to the presence of the oxide layer. Once the water vaporizes at T_v, the resulting vapor acts as oxidizer in the following zones. The end of Zone B is marked by the melting of the aluminum core at a temperature T_m. Melting of the aluminum core is followed by the cracking of oxide layer. Reactant molecules diffuse through these cracks and undergo reactions. Roughly around the end of Zone B and throughout Zone C, ignition reactions occur. Marking the end of Zone C, at temperature $T_{ign} = 1360$ K, overall ignition of the system is obtained. Zone D represents the flame zone leading to a flame temperature $T_f = 1800$ K.

The temperature profile, $T(x)$, and zone thicknesses, Δ, can be obtained by solving the energy equation in each zone and matching the physical conditions at the boundaries. The general equation of energy balance can be given as:

$$\frac{\partial}{\partial t}(\rho C_p T) = \frac{\partial}{\partial x}\left(k\frac{\partial T}{\partial x}\right) + \dot{Q}, \tag{12}$$

where ρ is the density, C_p is the specific heat, T is the temperature, k is the effective thermal conductivity of the mixture, and $\dot{Q}$ is the heat release rate (source term) which is zero in Zones A, B and C. Note that ρ, C_p, and k are functions of temperature and local mixture composition. In a flame coordinate system, assuming constant r_b, the partial time derivative, $\frac{\partial}{\partial t}$ can be written as $r_b \frac{d}{dx}$, and Eq. (12) can be rewritten as:

$$r_b \frac{d}{dx}(\rho C_p T) = \frac{d}{dx}\left(k\frac{dT}{dx}\right) + \dot{Q} \tag{13}$$

The linear burning rate, r_b, must be evaluated by the shooting method. Therefore, the first step is to assume an initial (guess solution) r_b. Neglecting the source term and expanding up the right hand side of the Eq. (13), the energy equation can be written as:

$$r_b \frac{d}{dx}(\rho C_p T) = \frac{dk}{dx} \cdot \frac{dT}{dx} + k\frac{d^2T}{dx^2}. \tag{14}$$

Eq. (14) can be discretized by one-dimensional finite difference method as:

$$r_b \frac{(\rho C_p T)_{i+1} - (\rho C_p T)_{i-1}}{2\Delta x} = \frac{k_{i+1} - k_{i-1}}{2\Delta x} \cdot \frac{T_{i+1} - T_{i-1}}{2\Delta x} + k_i \frac{T_{i+1} - 2T_i + T_{i-1}}{(\Delta x)^2}, \tag{15}$$

and solved using Gauss–Seidel iteration:

$$T_i^{n+1} = \frac{(\Delta x)^2}{2k_i}\left[\frac{k_{i+1}^n - k_{i-1}^n}{2\Delta x} \cdot \frac{T_{i+1}^n - T_{i-1}^n}{2\Delta x} + k_i \frac{T_{i+1}^n + T_{i-1}^n}{(\Delta x)^2} - r_b \frac{(\rho C_p T)_{i+1}^n - (\rho C_p T)_{i-1}^n}{2\Delta x}\right]. \tag{16}$$

Here i is the grid point index in the one-dimensional stencil consisting of $r+1$ grid points, and n denotes the iteration number. Note that the number of grid points should be chosen so as to include at minimum a full nanoparticle and the surrounding fluid medium. It is thus representative of the average mixture properties of the zone. If the grid size is smaller, then the effective thermal conductivity model fails for the control volume, leading to the failure of convergence of the iterative scheme. With the finite difference grid set up, the next step is to consider energy equations, identify boundary conditions, and perform the same numerical treatment for each zone present in the framework.

3.1. Energy balance for liquid water–solid aluminum (Zone A)

The liquid water zone is the region between $x = -\infty$ and $x = -\delta_v$. Here, the energy equation can be written as:

$$r_b \frac{d}{dx}\left[\left(\rho_{\mathrm{Al}} C_{p,\mathrm{Al}} \Phi_{\mathrm{Al}} + \rho_{ox} C_{p,ox} \Phi_{ox} + \rho_{lw} C_{p,lw} \Phi_{lw}\right) T\right] = \frac{d}{dx}\left(k_m \frac{dT}{dx}\right), \tag{17}$$

subject to boundary conditions: $T_{x\to-\infty} = T_u$; $T_{x=-\delta_v} = T_v$. The subscripts *Al, ox, lw,* and *m, W* denote aluminum, oxide layer, liquid water, and mixture in the liquid water zone, respectively. Assuming a zone length of ~1000 cm, and an initial linear temperature profile between the boundary conditions, $T_1 = T_u$ and $T_{r+1} = T_{vap}$, Eq. (16) is solved iteratively at each grid point until a steady state solution is obtained with a residual L_∞ norm less than 1×10^{-3}. Once the solution is obtained, the temperature gradient at the A–B interface ($x = -\delta_v$), $\frac{dT}{dx}|_W$ is calculated using a second order one-sided backward finite difference scheme. Using $\frac{dT}{dx}|_W$, the temperature gradient on the vapor side, $\frac{dT}{dx}|_V$, can be calculated as:

$$k_{m,AB+}\left.\frac{dT}{dx}\right|_V = k_{m,AB-}\left.\frac{dT}{dx}\right|_W + h_{fg}\Phi_{lw}\rho_{lw} r_b \tag{18}$$

where h_{fg} is the heat of vaporization of water, ρ_{lw} is the density of liquid water $T = T_{vap}$; Φ_{vap} is the mass fraction of water in the mixture and $k_{m,AB-}$ and $k_{m,AB+}$ are the thermal conductivities of the mixture to the left (liquid water) and right (vapor) of the phase boundaries respectively at $T = T_{vap}$.

3.2. Energy balance for water vapor–solid aluminum (Zone B)

The water vapor–solid aluminum mixture is encompassed by the region between $x = -\delta_v$ and $x = -\delta_m$. The energy equation in this region can be written in following form:

$$r_b \frac{d}{dx}\left[\left(\rho_{\mathrm{Al}} C_{p,\mathrm{Al}} \Phi_{\mathrm{Al}} + \rho_{ox} C_{p,ox} \Phi_{ox} + \rho_{lw} C_{p,wv} \Phi_{lw}\right) T\right] = \frac{d}{dx}\left(k_m \frac{dT}{dx}\right), \tag{19}$$

subject to the interfacial conditions:

$$\begin{cases} x = -\delta_v : T = T_v;\ k_{m+}\left.\dfrac{dT}{dx}\right|_V = k_{m-}\left.\dfrac{dT}{dx}\right|_W + h_{fg}\Phi_{lw}\rho_{lw} r_b \\ x = -\delta_m : T = T_m \end{cases}, \tag{20}$$

where the subscripts $-$ and $+$ represent the right and left side of the boundary AB respectively.

For Zone B, in addition to solving the temperature profile, we need to simultaneously determine the zone thickness, Δ_{BC}. For this, we first assume an initial zone thickness Δ_{BC} and then carry out a two-level iterative procedure – the inner level is to iteratively compute the temperature at each grid point using Eq. (16) and the outer level to correct the slope condition at the left boundary using a non-linear least square error minimization solver. The slope of the temperature profile at each outer step is computed from the converged temperature profile obtained from the inner step using a second order one-sided forward finite difference scheme. Once the converged zone thickness and corresponding temperature profile are simultaneously obtained, we can compute the heat flux at the right boundary, and thereafter compute the incoming heat flux from Zone C as:

$$k_{m,\mathrm{BC}+}\left.\frac{dT}{dx}\right|_{V,\mathrm{BC}+} = k_{m,\mathrm{BC}-}\left.\frac{dT}{dx}\right|_{V,\mathrm{BC}-} + h_{m\text{-}\mathrm{Al}}\Phi_{\mathrm{Al}}\rho_{\mathrm{Al}} r_b \tag{21}$$

where $h_{m\text{-Al}}$ is the heat of fusion of Al, ρ_{Al} is the density of solid Al at $T = T_m$, Φ_{Al} is the mass fraction of Al in the mixture, and $k_{m,\mathrm{BC}+}$and $k_{m,\mathrm{BC}-}$ are the thermal conductivities of the mixture corresponding to the left (solid Al) and right (molten Al) of the phase boundary respectively at $T = T_m$.

3.3. Energy balance for water vapor–molten aluminum (Zone C)

Like that for Zone B, the energy equation for Zone C can be written as:

$$r_b \frac{d}{dx}\left[\left(\rho_{l\mathrm{Al}} C_{p,l\mathrm{Al}} \Phi_{l\mathrm{Al}} + \rho_{ox} C_{p,ox} \Phi_{ox} + \rho_{lw} C_{p,wv} \Phi_{lw}\right) T\right] = \frac{d}{dx}\left(k_m \frac{dT}{dx}\right), \tag{22}$$

subject to the boundary conditions:

$$\begin{cases} x = -\delta_m : T = T_m;\ k_{m+}\left.\dfrac{dT}{dx}\right|_{V,m\mathrm{Al}} = k_{m-}\left.\dfrac{dT}{dx}\right|_V + h_{m\mathrm{Al}}\Phi_{\mathrm{Al}}\rho_{\mathrm{Al}} r_b, \\ x = 0 : T = T_{ign}, \end{cases} \tag{23}$$

where subscript *l*Al represents liquid aluminum and $h_{m\mathrm{Al}}$ is the enthalpy of fusion of aluminum.

A similar procedure followed for Zone B is used to compute the temperature profile and zone thickness Δ_{CD} of Zone C. The inner level computes the temperature profile for each estimate of zone thickness using Eq. (16) with $T_1 = T_m$ and $T_{r+1} = T_{\mathrm{ign}}$, and the outer level iteratively corrects the zone thickness to match the computed heat flux at the B–C interface from the inner step temperature profile with that obtained from Eq. (21). Finally, from the converged zone thickness and temperature profile, heat flux at the C–D interface, $k_{m,\mathrm{CD}-}\frac{dT}{dx}|_{V,\mathrm{CD}-}$ can be computed using a second order one-sided backward finite difference scheme. This heat flux is also equal to the heat flux coming in from the reaction Zone D, since there is no phase change associated with the C–D interface:

$$k_{m,\mathrm{CD}-}\left.\frac{dT}{dx}\right|_{V,\mathrm{CD}-} = k_{m,\mathrm{CD}+}\left.\frac{dT}{dx}\right|_{V,\mathrm{CD}+} \tag{24}$$

3.4. Energy balance for reaction zone (Zone D)

The energy equation for Zone D can be expressed as:

$$r_b \frac{d}{dx}\left[\left(\sum_i \rho_i C_{p,i} \Phi_i\right) T\right] = \frac{d}{dx}\left(k \frac{dT}{dx}\right) + \frac{\rho_m Q_r}{\tau_b}, \tag{25}$$

where Q_r is the chemical energy release per unit mass of the mixture, and τ_b is the particle burning time scale. The inputs required to solve these equations are physical properties: ρ and C_p, particle burning time τ_b, and mixture thermal conductivity k_m.

The thermophysical properties of aluminum and its oxide are taken from Refs. [46–48], and that of water and hydrogen are taken from Refs. [49,50]. The energy equation is modified to include the reaction source term and mean particle burning time as:

$$r_b \frac{d}{dx}(\rho C_p T) = \frac{dk_m}{dx}\left(\frac{\partial T}{\partial x}\right) + k_m \frac{d^2T}{dx^2} + \frac{Q_r \rho_m}{\tau_b}, \tag{26}$$

where Q_r is the heat released by combustion of unit mass of the stoichiometric mixture, ρ_m is the density of the mixture, and τ_b is a burning time parameter to characterize the rate of reaction. Since a detailed reaction mechanism of Al–H_2O combustion is yet to be developed, assuming a mean mass burning time scale is reasonable, as long as the experimental mass burning properties can be properly reproduced. Therefore, the particle burning time, τ_b, obtained from experimental measurements [10,51] is used. The mean particle burning time scale can be represented by the following equation:

$$\tau_b = \frac{c[a_1 \exp(b_1 T) + a_2 \exp(b_2 T)] d_p^2}{p^m}, \tag{27a}$$

$$m = a_3 \exp(b_3 T) + a_4 \exp(b_4 T) \tag{27b}$$

Table 1
Fitting constants in Eq. (27).

Constant	Value
c	1.736×10^{-3}
a_1	204.650
b_1	-9.848×10^{-3}
a_2	1.842×10^{-4}
b_2	3.461×10^{-5}
a_3	7.075
b_3	-1.905×10^{-3}
a_4	4.023×10^{-1}
b_4	-3.120×10^{-4}

where the burning time τ_b is in s, particle diameter d_p in nm and pressure p in atm. The numerical values corresponding to various fitting constants are given in Table 1.

Boundary conditions for solving the temperature profile and thickness of this zone are:

$$T_1 = T_{ig} \tag{28}$$

$$T_{r+1} = T_f \tag{29}$$

$$\left.\frac{dT}{dx}\right|_{r+1} = 0 \tag{30}$$

$$\left.\frac{dT}{dx}\right|_{1} = \left.\frac{dT}{dx}\right|_{CD+}. \tag{31}$$

Note, however, that for solving for temperature profile, only two boundary conditions are required, and for determining the reaction zone thickness, only one additional boundary condition is required. The fourth boundary condition can be used to correct the r_b, which was assumed at the very beginning of our calculations. Therefore, for Zone D, we follow a similar procedure as for Zones B and C, using an inner step with Eqs. (28) and (29) to solve Eq. (26) to determine the temperature profile for a given zone thickness, and an outer step to correct the zone thickness based on Eq. (30). Finally, r_b is estimated by iteratively solving the above steps (zones) until Eq. (31) is satisfied.

4. Results

4.1. Thermal transport

The thermal conductivity of nanoparticles can be derived from Eq. (32) as a function of temperature, size, and interfacial resistance obtained from the bulk thermal conductivity.

$$k_p = \frac{D_p}{\left(2.\frac{t_{ox}}{k_{Al_2O_3}} + \frac{D_{core}}{k_{Al}} + \frac{2}{G}\right)}, \tag{32}$$

where t_{ox} is the oxide layer thickness, and $D_{core} = D_p - 2.t_{ox}$ the diameter of the Al core. The thermal conductivity of bulk Al (not corrected for size effect), $k_{Al,uncorrected}$, is given as a function of temperature [32]:

$$\begin{aligned} &k_{Al,uncorrected}(T) = 3.101e^{-10}T^3 - 6.07e^{-7}T^2 + 3.271e^{-4}T + 0.186, \\ &\quad for\ T < T_{melt,Al} \\ &k_{Al,uncorrected}(T) = 7.5e^{-5}T + 0.025,\ for\ T \geq T_{melt,Al} \end{aligned} \tag{33}$$

Here $T_{melt,Al}$ is the melting point of bulk Al (=933 K). With the inclusion of size effects on thermal conductivity, the corrected k_{Al} becomes

$$\begin{aligned} &k_{Al}(T) = k_{Al,uncorrected}(T),\ D_{core} \geq 23\text{nm} \\ &k_{Al}(T) = \left(\tfrac{D_{core}}{23}\right)k_{Al,uncorrected}(T),\ D_{core} < 23\text{nm} \end{aligned} \tag{34}$$

Similarly, uncorrected thermal conductivity values of Al_2O_3 can be given as [33]:

$$k_{Al_2O_3,uncorrected}(T) = 65.08T^{-1.355} + 0.003441 \tag{35}$$

The correction on size effects results in:

$$\begin{aligned} &k_{Al_2O_3}(T) = k_{Al_2O_3,uncorrected}(T),\ t_{ox} \geq 47\text{nm} \\ &k_{Al_2O_3}(T) = \left(\frac{t_{ox}}{47}\right)k_{Al_2O_3,uncorrected}(T),\ t_{ox} < 47\text{nm} \end{aligned} \tag{36}$$

Muraleedharan et al. [52] have implemented ICMA calculations in an equilibrium molecular dynamics (EMD) framework for Al/Al_2O_3 system to evaluate G, and have achieved conclusive experimental validation for temperatures ranging from 50 to 500 K. They considered a (111) Al || (0001) Al_2O_3 crystal direction representing the primary orientation in FCC metal–metal oxide interface for both Al- and O-terminated Al_2O_3 surfaces. Here, the same ICMA framework is extended to temperatures up to 1800 K to evaluate G. Following the ICMA calculations, a temperature-dependent function of interfacial conductance, $G(T)$ was obtained by fitting a logarithmic curve to the data points using a least-square algorithm. Although the logarithmic function may not represent the actual physics of variation of G with T, it helps reduce fitting error. The model fitting errors for the above properties are well below 10%. $G(T)$ can be given as:

$$\begin{aligned} &G(T) = 137.72\log(T) - 492.32,\ \ for\ T < T_{melt,Al} \\ &G(T) = 40,\ for\ T \geq T_{melt,Al} \end{aligned} \tag{37}$$

In Eqs. (33)–(37), the unit of T is in K, t_{ox}, D_{core} in nm, k in kW/m K, and G in MW/m^2 K. Appropriate unit conversion is to be performed when using these values in Eq. (32).

Figure 5(a) shows the thermal resistance associated with Al and Al_2O_3 (evaluated using Eqs. (34) and (36)) and the interface resistance, $R(T) = 1/G(T)$. Figure 5(b) shows the percentage contribution of each thermal resistance to the total thermal resistance of the particle for temperatures ranging from 300 to 1800 K. The results correspond to a nanoparticle of diameter 38 nm coated by an oxide layer of initial thickness 2.7 nm, which increases as the reaction proceeds. As can be seen from Fig. 5(a), TIR decreases monotonically with temperature to the melting temperature of Al = 933 K. At the melting temperature, there is a sharp rise in TIR, which remains nearly constant thereafter. This is due to the loss of crystallinity of the core Al lattice as it melts. The thermal resistance of Al_2O_3, on the other hand, shows a monotonically increasing trend as it remains in solid state throughout the temperature range considered. Its increase is a combined result of the decrease in thermal conductivity and the increase in oxide layer thickness. Note that, for most temperatures, TIR is higher than Al_2O_3 resistance, which indicates that TIR is crucial in modeling the net thermal resistance of the nanoparticle. Moreover, from Fig. 5(a), it is quite evident that the Al contribution to total resistance is the lowest. Thermal resistance of Al is two orders of magnitude lower than that of Al_2O_3 and the interface. In other words, Al offers the highest conductive pathway for energy released at the reaction zone to traverse through the unburnt mixture. Had the oxide layer been absent from the Al surface, the medium would have offered much lower resistance to heat conduction, and would have had a much higher burning rate. In liquid state, as at the interface, Al also offers significantly higher resistance, due to lack of crystallinity. Furthermore, from Fig. 5(b), comparing the percentage contribution of each of the components, it is evident that TIR and the oxide layer resistance together contribute to > 95% of thermal resistance. Now the same approach can be extended to various particle sizes and

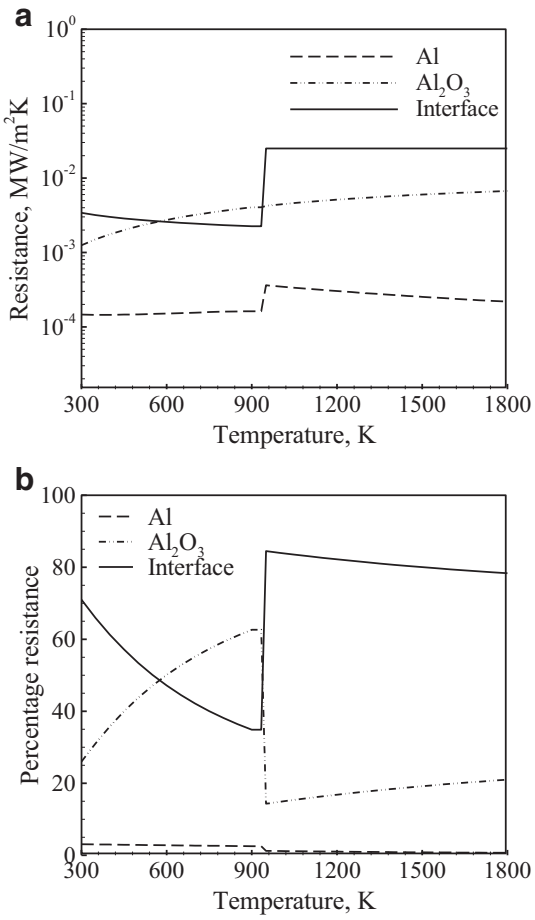

Fig. 5. (a) Thermal resistance of Al, Al_2O_3, and interface (b) percentage contribution of each resistance component to the total thermal resistance of the nanoparticle.

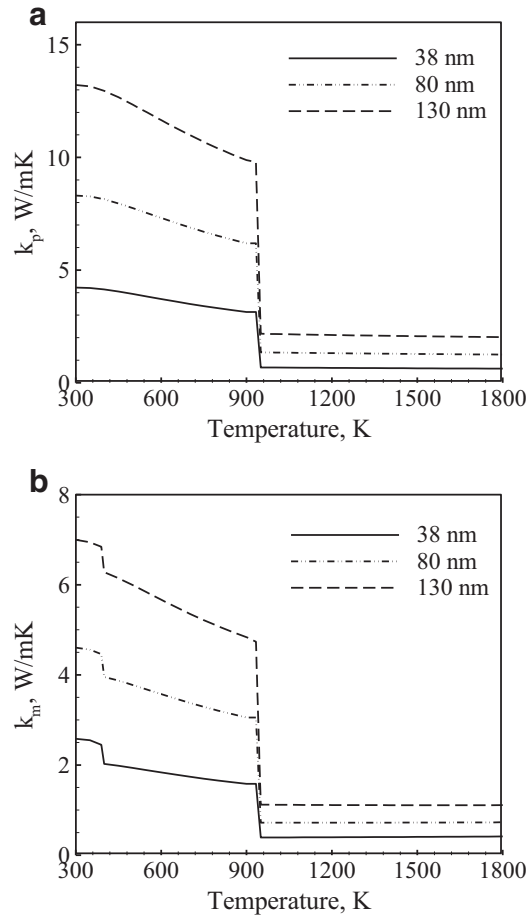

Fig. 6. (a) Thermal conductivity of nanoparticles of diameters $D_p = 38$ nm, 80 nm, and 138 nm, and (b) effective thermal conductivity of nAl-H_2O mixture, as a function of temperature.

used in conjunction with the MEB model given in Eq. (10) to predict the thermal conductivity of the mixture.

Utilizing the temperature-dependent thermal resistance values depicted in Fig. 5(a), particle thermal conductivity, k_p is evaluated using Eq. (32) for three different particle diameters D_p: 38 nm, 80 nm, and 138 nm.

Figure 6(a) shows k_p as a function of temperature. As can be seen from Fig. 6(a), k_p decreases steadily with temperature, drops sharply at the melting temperature of Al, and remains nearly constant thereafter. Using the particle and fluid thermal conductivities, the effective thermal conductivity of the mixture, k_m can be evaluated using the MEB model. Results of the temperature dependent k_m for different particle sizes are shown in Fig. 6(b). In addition to the decreasing trend in k_m, two sharp drops are also observed, corresponding to the vaporization temperature of water at 373 K and the melting point of Al, respectively. More importantly, k_m increases with an increase in particle size, because the thermal resistance of core Al decreases. Results shown in Fig. 6 are obtained straightforwardly from Eqs. (32) and (10), and need to be validated against experimental measurements by applying the numerical framework to predict burning properties.

4.2. Flame propagation

A numerical solution of the flame problem yields the temperature profile across the reaction and preheat zones, as shown in Fig. 7. Figure 7 represents Zones A–D in the multizone framework corresponding to a baseline case of 38 nm particle suspension at pressure, $P = 1$ bar. Results for r_b and thicknesses of various zones

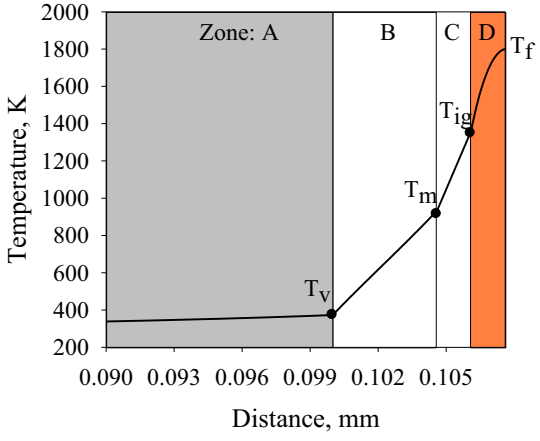

Fig. 7. Detailed flame structure obtained via numerical solution of the 1D flame propagation problem, clearly showing the different zones and their thicknesses.

are given in Table 2. r_b predicted for the baseline case is 1.79 cm/s, and the two sets of experimental measurements [28] give a value of ~1.61 cm/s and ~1.40 cm/s, respectively. Error in r_b predictions is < 10%, demonstrating the fidelity of the numerical framework. Prior theoretical studies [10] severely overpredict r_b as 4.4 cm/s, because they do not account for interface resistance, size-effects, and spatial variation of thermal transport properties. The thicknesses of Zones B, C, and D are also obtained as 4.7 μm, 1.01 μm,

Table 2
Summary of results obtained from numerical solution of flame structure and burning properties for baseline case ($P = 1$ bar; $D_p = 38$ nm), compared with experimental results [10] and prior theoretical model [10].

Linear burning rate, r_b	Zone B	Zone C	Zone D
Present work = 1.79 cm/s	4.7 μm	1.01 μm	1.49 μm
Expt 1: 1.61 cm/s [28]			
Expt 2:1.40 cm/s [28]			
Prior work: 4.4 cm/s [10]			

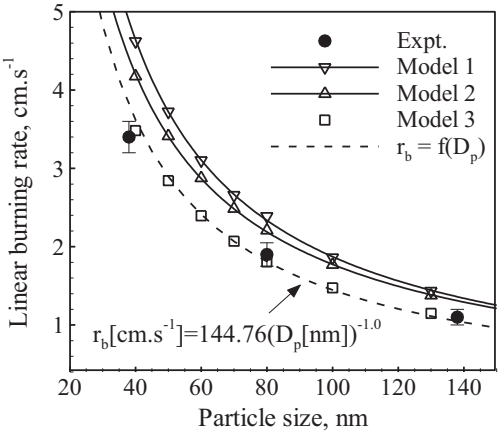

Fig. 8. Linear burning rate, r_b as a function of particle diameter; r_b is predicted using increasing levels of complexity in modeling particle thermal conductivity.

and 1.49 μm, respectively. Zone thicknesses elucidate finer details of the flame structure that are difficult to measure experimentally. Also note that the slope of the temperature profile increases at the point where it crosses the A–B interface, accounting for the enthalpy of vaporization of water. A similar increase in slope is observed at B–C, where it accounts for enthalpy of fusion of Al. The end of Zone D is marked by a zero slope, corresponding to constant flame temperature, T_f, as there is no heat transfer between reaction zone and products.

Having the numerical framework benchmarked with baseline experimental results, a detailed analysis of r_b as a function of k_p modeled with increasing levels of complexity is studied. Figure 8 compares r_b predicted using 3 different k_p models at $P = 10$ bar. Model 1 includes only the thermal conductivity of Al, k_{Al}, to represent k_p. This model neglects the presence of the oxide layer and, therefore, chooses the highest thermal conduction pathway. In Model 2, the Al core and the oxide layer are considered but TIR is neglected. Model 3 has the highest complexity; TIR is also used to model k_p. In Fig. 8, experimentally measured r_b values are also overlaid for comparison [28]; the predictions of Model 3 are closer to the experimental values. Models 1 and 2 overpredict r_b, because they intrinsically model a higher thermal conductivity for the mixture. The mean error in Model 1 is ~20%, whereas in Model 2 it decreases to ~18%. The mean error in Model 3 is < 5% and the maximum error in the prediction is ~12% for $D_p = 38$ nm. A model fit on r_b v/s D_p predicted from Model 3 obtained from the least squares algorithm gives a relation: $r_b[\text{cm.s}^{-1}] = 144.76(D_p[\text{nm}])^{-1.0}$. Hence, r_b is inversely proportional to D_p, which is in accordance with the experimental measurements [27].

Finally, we study the sensitivity of r_b to changes in the thermal conductivity of Al and Al_2O_3, and G at $P = 10$ bar. This study is motivated by recent advances in nanotechnology, whereby thermal conductivity can be tuned by rational design of materials, i.e., by engineering features to target a certain group of vibrational modes to either inhibit or enhance their role in heat conduction [53,54].

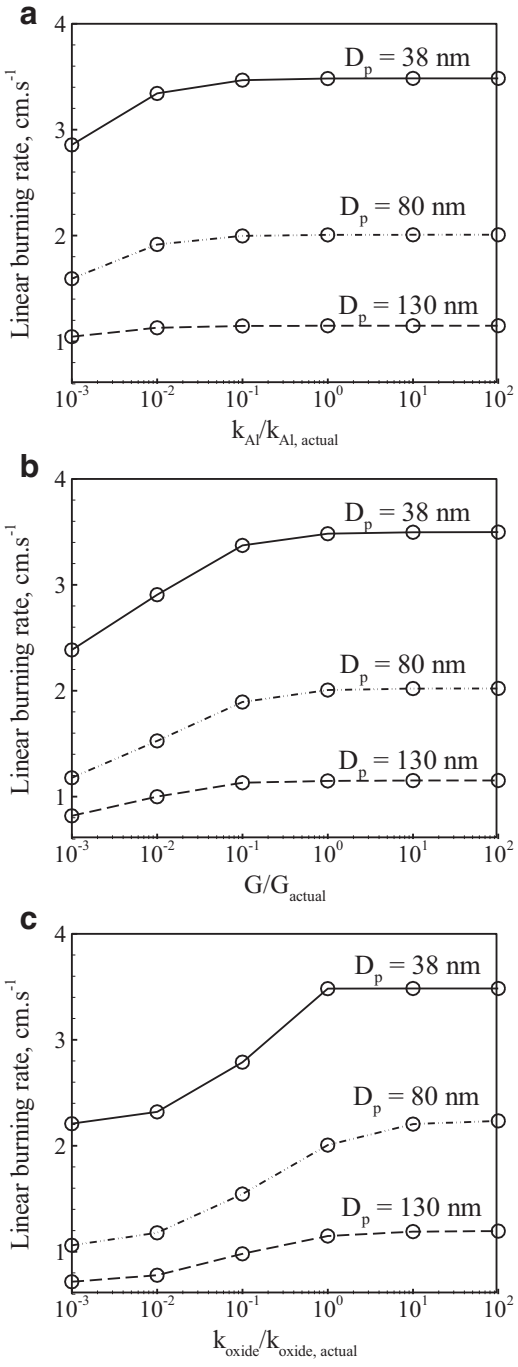

Fig. 9. Sensitivity of linear burning rate to changes in thermal conductivity of (a) Al and (b) Al_2O_3, and (c) thermal interfacial conductance, G, for three different particle sizes.

Tuning thermal conductivity provides means to precisely control the burning rates of energetic materials in propulsive missions. Here, the individual thermal conductivity components k_{Al}, G, and $k_{Al_2O_3}$ are arbitrarily varied with respect to their actual values and the effects on r_b are analyzed. Figure 9(a)–(c) present the sensitivity of r_b to changes in k_{Al}, G, and $k_{Al_2O_3}$, respectively.

From Fig. 9(a)–(c), it is evident that in general, r_b sensitivity is highest for 38 nm particle suspensions. From Fig. 9(a), it can be seen that for $D_p = 38$ nm, for two orders of magnitude reduction in k_{Al}, reduction in r_b is only ~15%, whereas, Fig. 9(b) indicates that for the same reduction in G, the reduction in r_b is nearly ~30%. On the other hand, Fig. 9(c) clearly shows that r_b drops by ~34%

when $k_{Al_2O_3}$ decreases by two orders of magnitude. It is, therefore, quite evident that the thermal conductivity of the oxide layer and interface conductance dictate r_b sensitivity. While $k_{Al_2O_3}$ seems to have the highest influence on r_b, it is also important to note that the oxide layer forms on the particle surface in situ during the combustion process, and its thermal conductivity is practically uncontrollable. TIC, on the other hand, can be tuned to user requirements if certain vibrational modes in the Al core are preferentially altered by means of nanoengineered defects, doping, and/or alloying. In other words, precise tuning of burning rate in nanoenergetic materials is achievable by careful consideration of interfacial conductance. Nonetheless, as particles become larger, sensitivity of r_b to changes in k seems to diminish. Note that for all particle sizes, even with several-fold enhancement in k and G, the effect on r_b is feeble. Therefore, to increase burning rates in nanoenergetic materials, conventional strategies to improve reaction rates, like high pressure combustion, active metal coating, or catalysis, must be adopted.

5. Conclusions

A detailed numerical analysis of flame propagation in nano-aluminum (nAl)–water (H_2O) mixtures is performed. Considering a multi-zone framework, the nonlinear energy equation is solved iteratively using the Gauss–Seidel method. The thermal conductivity of the nanoparticle is modeled using the thermal conductivities of the aluminum and oxide layer, as well as the thermal interface resistance. Effective thermal conductivity of the mixture is modeled using the Maxwell–Eucken–Bruggeman model, as a function of temperature, spatial coordinate, and local mixture composition. Results indicate that the oxide layer and the interface together contribute around 95% of the net thermal resistance of the nanoparticle. The effect of complexity in modeling particle thermal conductivity, k_p, was studied by predicting the particle size-dependent linear burning rate, r_b. Error in r_b prediction is lowest ($<5\%$) when interface resistance is taken into account in modeling k_p. When interface resistance is neglected, error in r_b prediction increases to 20%. Furthermore, r_b varies as the inverse of particle diameter, as observed in experimental measurements. The sensitivity of r_b to changes in the thermal conductivities of aluminum (k_{Al}) and aluminum oxide ($k_{Al_2O_3}$), and interface conductance (G) is also studied for three particle sizes: 38 nm, 80 nm, and 138 nm. r_b sensitivity is the highest for the 38 nm particle, and it decreases with increase in particle size. r_b drops by 15%, 30%, and 34% for two orders of magnitude reduction in k_{Al}, G, and $k_{Al_2O_3}$, respectively. No notable enhancement in r_b is achieved by an enhancement in thermal conductivity or interface conductance.

Acknowledgments

This work was sponsored by the Air force Office of Scientific Research under contract no. FA-9550-13-1-0004. The support and encouragement provided by Dr. Mitat A. Birkan is gratefully acknowledged.

References

[1] V. Yang, Solid propellant chemistry combustion and motor interior ballistics, Prog. Astronaut. Aeronaut. AIAA 185 (2000) 663.
[2] J. Foote, B. Thompson, J. Lineberry, Combustion of aluminum with steam for underwater propulsion, Adv. Chem. Propuls. (2001) 133–145.
[3] P. Brousseau, C.J. Anderson, Nanometric aluminum in explosives, Propellants Explos. Pyrotech. 27 (2002) 300–306.
[4] E. Shafirovich, V. Diakov, A. Varma, Combustion of novel chemical mixtures for hydrogen generation, Combust. Flame 144 (2006) 415–418.
[5] D. Sundaram, V. Yang, R.A. Yetter, Metal-based nanoenergetic materials: synthesis, properties, and applications, Prog. Energy Combust. Sci. 61 (2017) 293–365.
[6] D.S. Sundaram, P. Puri, V. Yang, A general theory of ignition and combustion of nano-and micron-sized aluminum particles, Combust. Flame 169 (2016) 94–109.
[7] E.W. Price, R.K. Sigman, Combustion of aluminized solid propellants, solid propellant chemistry, combustion, and motor interior ballistics, Prog. Astronaut. Aeronaut. AIAA 185 (2000) 663–687.
[8] D. Sundaram, V. Yang, V. Zarko, Combustion of nano aluminum particles (review), Combust. Explos. Shock Waves 51 (2014) 173–196.
[9] D.S. Sundaram, V. Yang, Effect of packing density on flame propagation of nickel-coated aluminum particles, Combust. Flame 161 (2014) 2916–2923.
[10] D.S. Sundaram, V. Yang, Y. Huang, G.A. Risha, R.A. Yetter, Effects of particle size and pressure on combustion of nano-aluminum particles and liquid water, Combust. Flame 160 (2013) 2251–2259.
[11] R. Duffin, L. Tran, D. Brown, V. Stone, K. Donaldson, Proinflammogenic effects of low-toxicity and metal nanoparticles in vivo and in vitro: highlighting the role of particle surface area and surface reactivity, Inhal. Toxicol. 19 (2007) 849–856.
[12] P. Puri, V. Yang, Effect of particle size on melting of aluminum at nano scales, J. Phys. Chem. C 111 (2007) 11776–11783.
[13] Y. Huang, G.A. Risha, V. Yang, R.A. Yetter, Effect of particle size on combustion of aluminum particle dust in air, Combust. Flame 156 (2009) 5–13.
[14] D.G. Cahill, P.V. Braun, G. Chen, D.R. Clarke, S. Fan, K.E. Goodson, P. Keblinski, W.P. King, G.D. Mahan, A. Majumdar, H.J. Maris, S.R. Phillpot, E. Pop, L. Shi, Nanoscale thermal transport. II. 2003–2012, Appl. Phys. Rev. 1 (2014) 011305.
[15] K. Esfarjani, J. Garg, G. Chen, Modeling heat conduction from first principles, Annu. Rev. Heat Transf. 17 (2014) 9–47.
[16] G. Chen, Nanoscale energy transport and conversion: a parallel treatment of electrons, molecules, phonons, and photons, Oxford University Press, 2005.
[17] M.A. Trunov, M. Schoenitz, E. Dreizin, Effect of polymorphic phase transformations in alumina layer on ignition of aluminium particles, Combust. Theory Model. 10 (2006) 603–623.
[18] A. Rai, D. Lee, K. Park, M.R. Zachariah, Importance of phase change of aluminum in oxidation of aluminum nanoparticles, J. Phys. Chem. B 108 (2004) 14793–14795.
[19] G. Chen, Phonon heat conduction in nanostructures, Int. J. Therm. Sci. 39 (2000) 471–480.
[20] G. Chen, Particularities of heat conduction in nanostructures, J. Nanopart. Res. 2 (2000) 199–204.
[21] M. Hu, P. Keblinski, J.-S. Wang, N. Raravikar, Interfacial thermal conductance between silicon and a vertical carbon nanotube, J. Appl. Phys. 104 (2008) 083503.
[22] M. Hu, S. Shenogin, P. Keblinski, Molecular dynamics simulation of interfacial thermal conductance between silicon and amorphous polyethylene, Appl. Phys. Lett. 91 (2007) 241910.
[23] R. Stoner, H. Maris, Kapitza conductance and heat flow between solids at temperatures from 50 to 300K, Phys. Rev. B 48 (1993) 16373.
[24] P.E. Hopkins, T. Beechem, J.C. Duda, K. Hattar, J.F. Ihlefeld, M.A. Rodriguez, E.S. Piekos, Influence of anisotropy on thermal boundary conductance at solid interfaces, Phys. Rev. B 84 (2011) 125408.
[25] P.E. Hopkins, R. Salaway, R. Stevens, P. Norris, Temperature-dependent thermal boundary conductance at Al/Al_2O_3 and Pt/Al_2O_3 interfaces, Int. J. Thermophys. 28 (2007) 947–957.
[26] H. Tyagi, P.E. Phelan, R. Prasher, R. Peck, T. Lee, J.R. Pacheco, P. Arentzen, Increased hot-plate ignition probability for nanoparticle-laden diesel fuel, Nano Lett. 8 (2008) 1410–1416.
[27] G.A. Risha, S.F. Son, R. Yetter, V. Yang, B. Tappan, Combustion of nano-aluminum and liquid water, Proc. Combust. Inst. 31 (2007) 2029–2036.
[28] G.A. Risha, J.L. Sabourin, V. Yang, R.A. Yetter, S.F. Son, B.C. Tappan, Combustion and conversion efficiency of nanoaluminum–water mixtures, Combust. Sci. Technol. 180 (2008) 2127–2142.
[29] K. Gordiz, A. Henry, A formalism for calculating the modal contributions to thermal interface conductance, New J. Phys. 17 (2015) 103002.
[30] M.G. Muraleedharan, A. Rohskopf, V. Yang, A. Henry, Phonon optimized interatomic potential for aluminum, AIP Adv. 7 (2017) 125022.
[31] A. Jain, A.J. McGaughey, Thermal transport by phonons and electrons in aluminum, silver, and gold from first principles, Phys. Rev. B 93 (2016) 081206.
[32] S. Abu-Eishah, Correlations for the thermal conductivity of metals as a function of temperature, Int. J. Thermophys. 22 (2001) 1855–1868.
[33] Y.S. Touloukian, Thermophysical properties of high temperature solid materials. Volume 4. Oxides and their solutions and mixtures. Part 1. Simple oxygen compounds and their mixtures, Thermophysical and Electronic Properties Information Analysis Center Lafayette In, 1966.
[34] J.-L. Barrat, F. Chiaruttini, Kapitza resistance at the liquid—solid interface, Mol. Phys. 101 (2003) 1605–1610.
[35] G. Domingues, S. Volz, K. Joulain, J.-J. Greffet, Heat transfer between two nanoparticles through near field interaction, Phys. Rev. Lett. 94 (2005) 085901.
[36] R. Kubo, The fluctuation-dissipation theorem, Rep. Prog. Phys. 29 (1966) 255.
[37] X.F. Zhou, L. Gao, Effective thermal conductivity in nanofluids of nonspherical particles with interfacial thermal resistance: differential effective medium theory, J. Appl. Phys. 100 (2006) 024913.
[38] W. Yu, S. Choi, The role of interfacial layers in the enhanced thermal conductivity of nanofluids: a renovated Maxwell model, J. Nanopart. Res. 5 (2003) 167–171.
[39] C.-W. Nan, R. Birringer, D.R. Clarke, H. Gleiter, Effective thermal conductivity of particulate composites with interfacial thermal resistance, J. Appl. Phys. 81 (1997) 6692–6699.

[40] P. Keblinski, S. Phillpot, S. Choi, J. Eastman, Mechanisms of heat flow in suspensions of nano-sized particles (nanofluids), Int. J. Heat Mass Transf. 45 (2002) 855–863.
[41] M.G. Muraleedharan, D.S. Sundaram, A. Henry, V. Yang, Thermal conductivity calculation of nano-suspensions using Green–Kubo relations with reduced artificial correlations, J. Phys.: Condens. Matter 29 (2017) 155302.
[42] J. Wang, J.K. Carson, M.F. North, D.J. Cleland, A new approach to modelling the effective thermal conductivity of heterogeneous materials, Int. J. Heat Mass Transf. 49 (2006) 3075–3083.
[43] A. Eucken, Allgemeine gesetzmäßigkeiten für das wärmeleitvermögen verschiedener stoffarten und aggregatzustände, Forsch. Geb. Ing. A 11 (1940) 6–20.
[44] J.C. Maxwell, A treatise on electricity and magnetism, Clarendon Press, 1881.
[45] V.D. Bruggeman, Berechnung verschiedener physikalischer konstanten von heterogenen substanzen. I. Dielektrizitätskonstanten und leitfähigkeiten der mischkörper aus isotropen substanzen, Ann. Phys. 416 (1935) 665–679.
[46] W. Gale, T. Totemeier, Smithells metals reference book, Eight edition, Oxford, Amsterdam, Boston, Heidelberg, London, New York, 2004.
[47] E.H. Buyco, F.E. Davis, Specific heat of aluminum from zero to its melting temperature and beyond. Equation for representation of the specific heat of solids, J. Chem. Eng. Data 15 (1970) 518–523.
[48] M. Munro, Evaluated material properties for a sintered alpha-alumina, J. Am. Ceram. Soc. 80 (1997) 1919–1928.
[49] J. Sengers, J.T.R. Watson, Improved international formulations for the viscosity and thermal conductivity of water substance, J. Phys. Chem. Ref. Data 15 (1986) 1291–1314.
[50] E. Lemmon, M. Huber, M. McLinden, REFPROP: Reference fluid thermodynamic and transport properties, NIST Stand. Ref. Datab. 23 (2007).
[51] T. Bazyn, H. Krier, N. Glumac, Combustion of nanoaluminum at elevated pressure and temperature behind reflected shock waves, Combust. Flame 145 (2006) 703–713.
[52] M.G. Muraleedharan, K. Gordiz, S. Ju, J. Shiomi, V. Yang, A. Henry, Thermal interface conductance between aluminum and aluminum oxide: a rigorous test of atomistic level theories, arXiv Preprint (2018).
[53] T. Kodama, M. Ohnishi, W. Park, T. Shiga, J. Park, T. Shimada, H. Shinohara, J. Shiomi, K.E. Goodson, Modulation of thermal and thermoelectric transport in individual carbon nanotubes by fullerene encapsulation, Nat. Mater. 16 (2017) 892.
[54] S. Ju, T. Shiga, L. Feng, Z. Hou, K. Tsuda, J. Shiomi, Designing nanostructures for phonon transport via Bayesian optimization, Phys. Rev. X 7 (2017) 021024.